ADVANCED MATERIALS
www.advmat.de

Wood-Inspired High-Performance Ultrathick Bulk Battery Electrodes

Lei-Lei Lu, Yu-Yang Lu, Zi-Jian Xiao, Tian-Wen Zhang, Fei Zhou, Tao Ma, Yong Ni, Hong-Bin Yao, Shu-Hong Yu,* and Yi Cui**

Ultrathick electrode design is a promising strategy to enhance the specific energy of Li-ion batteries (LIBs) without changing the underlying materials chemistry. However, the low Li-ion conductivity caused by ultralong Li-ion transport pathway in traditional random microstructured electrode heavily deteriorates the rate performance of ultrathick electrodes. Herein, inspired by the vertical microchannels in natural wood as the highway for water transport, the microstructures of wood are successfully duplicated into ultrathick bulk $LiCoO_2$ (LCO) cathode via a sol–gel process to achieve the high areal capacity and excellent rate capability. The X-ray-based microtomography demonstrates that the uniform microchannels are built up throughout the whole wood-templated LCO cathode bringing in 1.5 times lower of tortuosity and ≈2 times higher of Li-ion conductivity compared to that of random structured LCO cathode. The fabricated wood-inspired LCO cathode delivers high areal capacity up to 22.7 mAh cm^{-2} (five times of the existing electrode) and achieves the dynamic stress test at such high areal capacity for the first time. The reported wood-inspired design will open a new avenue to adopt natural hierarchical structures to improve the performance of LIBs.

The critical demands for high energy/power density of energy storage devices are requiring the upgrade of current technologies of Li-ion batteries (LIBs).[1–3] In past years, to boost the development of LIBs, most of studies were focused on searching novel electrode materials aiming to replace the low capacity materials already used in commercial batteries,[4,5] whereas the equally efficient strategy to optimize the performance of LIBs via the electrode microstructural engineering attracted less attention. In presently commercial LIBs, the thickness of electroactive components including the cathode and the anode are both limited between 50 and 100 μm.[6] Thus, there is much space to improve the energy density of given electrochemically coupled cell by enhancing the volume ratio of active materials to inactive materials through increasing the thickness of electrodes.[7,8]

Importantly, recent studies have shown that the microstructure of electrode can significantly impact the performance metrics of LIBs,[9–11] which afforded us a promising route to fabricate high energy/power density LIBs via microstructure engineered ultrathick and high rate electrodes instead of changing the underlying materials chemistry. However, efforts to enhance the performance of LIBs toward thicker, higher mass-per-areal of electrochemically active materials are challenging mainly due to the ultralong Li-ion transport pathway and high resistance of the diffusion of Li ions in ultrathick electrode, especially for the cell operated at high rates.[11–13]

To achieve efficient ultrathick electrode design, the electrode tortuosity (τ) and electrode porosity (ε) are determining factors because they are highly relative to Li-ion conductivity and specific capacity of electrodes. It has been demonstrated that the tortuosity is heavily affected by the microstructure of the electrode and has significant impact on the rate capability of LIBs.[11,14–17] In past decades, various microstructures of electrodes to minimize the tortuosity for improving the rate capabilities of LIBs have been explored.[18–21] Previous attempts to obtain low-tortuosity electrode focused on the multimodal/hierarchical porous network[22,23] for high rate performance. Recently, the construction of electrode microstructure with directional microchannels aligned in the Li-ion transport direction has been adopted as an efficient strategy for achieving the low tortuosity in thick electrode. Up to now, only the vertical ice templating and magnetic field controlled assembly of $LiCoO_2$ (LCO) nanoparticles into directional alignments have been developed to fabricate thick LCO electrodes with low tortuosity and high rate performance.[24–26]

Dr. L.-L. Lu, Dr. Y.-Y. Lu, Dr. Z.-J. Xiao, Dr. T.-W. Zhang, Dr. F. Zhou, Dr. T. Ma, Prof. Y. Ni, Prof. H.-B. Yao, Prof. S.-H. Yu
Division of Nanomaterials and Chemistry
Hefei National Research Center for Physical Sciences at the Microscale
CAS Center for Excellence in Nanoscience
Collaborative Innovation Center of Suzhou Nano Science and Technology
Department of Chemistry
Hefei Science Center of CAS
University of Science and Technology of China
Hefei, Anhui 230026, China
E-mail: yhb@ustc.edu.cn; shyu@ustc.edu.cn
Prof. Y. Cui
Department of Materials Science and Engineering
Stanford University
Stanford, CA 94305, USA
E-mail: yicui@stanford.edu
The ORCID identification number(s) for the author(s) of this article can be found under https://doi.org/10.1002/adma.201706745.

DOI: 10.1002/adma.201706745

 © 2018 WILEY-VCH Verlag GmbH & Co. KGaA, Weinheim

Ningde Amperex Tech. Exhibit No. 2036
Zhuhai CosMX Battery Co. Ltd. v. Ningde Amperex Tech.
IPR2025-00431, U.S. Patent No. 11,799,131
Page 1 of 9

To explore the potentials of engineered ultrathick electrode design for improving the energy/power density of LIBs, more general and sustainable approaches are highly desired to fabricate uniformly aligned microchannels in the electrode. To build up hierarchical microstructures for improving the performance of materials, nature has provided us many templates and material design inspirations.[27–30] For example, the "brick and mortar" layered microstructure in nacre has inspired us to fabricate various artificial engineered materials with high mechanical performances.[31–34] For the typical microstructural model with low tortuosity, the vertical microchannels widely exist in natural woods as high pathway for the transportation of water, which has inspired the fabrication of hierarchically structured engineering ceramics with improved mechanical strength[35,36] and the carbon-based current collectors.[37]

Herein, we report a wood-inspired route to fabricate ultrathick LCO cathode with directional microchannel alignments to reduce the tortuosity for improving the areal capacity and rate capability of LCO cathode. Through a facile sol–gel infiltration and subsequent calcination process, we can completely duplicate the vertical microchannel structures of wood into free-standing bulk LCO cathode with the thickness up to 1 mm, more than ten times of the existing electrodes. Due to the well-defined microchannels in the obtained bulk LCO cathode, the conductivity of Li ions in this electrode was largely improved compared to that of traditional LCO cathode consisting of randomly dispersed LCO particles. The areal capacity of as-fabricated bulk LCO cathode reached up to as high as 22.7 mAh cm^{-2} under the conditions of dynamic stress test (DST), which is, to our best knowledge, the highest areal capacity of LCO cathode reported presently.

The wood displays anisotropic structure with vertical microchannels serving as the high transport pathway of water from the root to the crown (**Figure 1**a). Inspired by this structure, we developed a natural wood templating technique to fabricate ultrathick LCO cathode inheriting the typical microstructures with low tortuosity to facilitate Li-ion transport in the electrode. In traditional LCO electrode, the active LCO particles were connected by conductive carbon black and polymer binders in a random architecture resulting in poor electrolyte diffusion and long Li-ion transport pathway (Figure 1b). In contrast, the uniform microchannels in the wood-inspired LCO cathode endow the reduced tortuosity to improve the electrolyte diffusion and shorten the Li-ion transport distance in the electrode (Figure 1c). With this wood-inspired microstructure design to overcome the limitation of Li-ion transport, it is feasible to increase the thickness of LCO cathode without reducing its rate performance. In this case, it is possible to fabricate the LCO cathode with the thickness up to 1 mm, ≈12 times of the thickness of commercial LCO electrode (Figure 1d). Along with the thickness increase of LCO cathode, the specific energy of LIB is correspondingly significantly improved at all levels of porosity in LCO cathode (for the details of the evaluation, please see Supporting Information). The variation trends of the calculated specific energy of LCO-graphite LIBs with the increase in thickness of electrodes at different porosities are plotted in Figure 1e. In a typical example, with the 60% porosity of electrode, the specific energy of LCO-graphite LIBs increased from ≈260 to 350 Wh kg^{-1} when the thickness of electrode increased ten times, implying the significant contribution of the thickness increase of electrodes to enhancing the energy density of LIBs.

LCO is one of the most attractive cathodes to fabricate ultrathick electrode due to its relatively high compaction density, moderate electronic conductivity, and good cycling stability.[38] The vertical microchannels exist widely in woods such as basswood and pinewood (Figure S1, Supporting Information). Given the similarity of the microstructures of wood templates, the pinewoods (pinus sylvestris var. mongolica) were used as templates for our work due to their wide availability. As shown in **Figure 2**a, the ultrathick LCO cathode is fabricated via a facile sol–gel vacuum-assisted infusion and calcination process based on the pinewood template. A wood block was first cut into square slices with the thickness of 1.5 mm and then

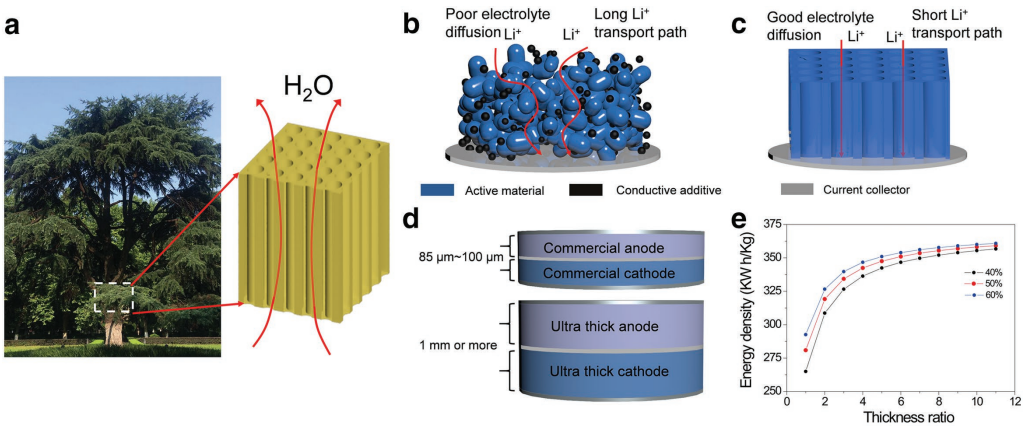

Figure 1. Wood-inspired design for ultrathick electrodes. a) The Photograph of pinewood and the illustration of the wood anisotropic structure for the transport of water. b) The illustration of traditional electrode with poor electrolyte diffusion and long Li-ion transport path. c) The illustration of wood-inspired electrode with vertical channels to shorten the Li-ion transport path. d) The model illustration for the comparison of commercial electrode and ultrathick electrode. e) The plot of the trends of the increase of energy density of LCO-graphite cell with the increase of the thickness of electrodes at different porosities.

© 2018 WILEY-VCH Verlag GmbH & Co. KGaA, Weinheim

Ningde Amperex Tech. Exhibit No. 2036
Zhuhai CosMX Battery Co. Ltd. v. Ningde Amperex Tech.
IPR2025-00431, U.S. Patent No. 11,799,131
Page 2 of 9

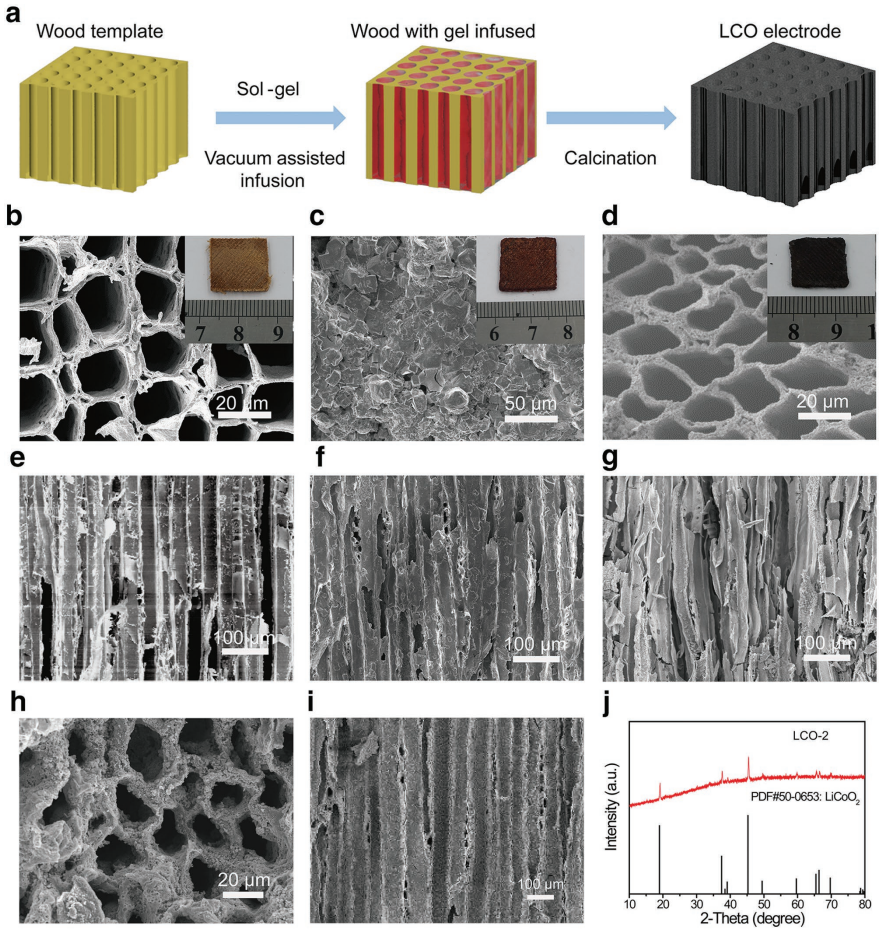

Figure 2. The fabrication and characterization of ultrathick bulk LCO cathodes by wood templating. a) The illustration of fabrication procedure of ultrathick LCO cathode by wood templating. b,e) The top view (b) and cross-section view (e) of original wood, respectively. c,f) The top view (c) and cross-section view (f) of original wood after sol infusion and gel formation, respectively. d,g) The top view (d) and cross-section view (g) of LCO-1 electrode, respectively. The inserts in b–d are corresponding photos of samples. h,i) The top view (h) and cross-section view (i) of LCO-2 electrode, respectively. j) PXRD pattern of as-obtained LCO-2 cathode.

the lignin in the microchannels of wood slices was removed via ammonia solution treatment (Figure S2, Supporting Information). The pinewood slice after ammonia solution treatment has an area of 15 × 15 mm with a thickness of 1.5 mm (Figure S3, Supporting Information). The scanning electron microscopy (SEM) images of pinewood slices before and after ammonia solution treatment demonstrated its enhanced pore connectivity after removal of lignin (Figure S4, Supporting Information). The obtained pinewood slice (inset in Figure 2b) exhibited highly uniform porous structures with the diameter of around 30–40 μm (Figure 2b). The cross-sectional SEM image (Figure 2e) further shows that the vertical microchannels are continuously aligned throughout the pinewood slice. The LCO precursor sol was easily infiltrated into the microchannels of pinewood slice under the assistance of vacuum. After the infusion of LCO precursor sol, the infiltrated pinewood slice was heated in the vacuum oven at 90 °C for 72 h to evaporate the solvent, resulting in the transformation of sol into the gel. With the formation of LCO precursor gel, the color of pinewood slice changed to dark red (Inset in Figure 2c) and the excess gel covered on the surface of pinewood slice (Figure S5a, Supporting Information) due to the volume expansion in the process of gel formation,[39] implying that the gel was fully filled into the microchannels of pinewood slice. The infiltration of LCO gel into the microchannels was further confirmed by the SEM characterization. As shown in Figure 2c, the pores of microchannels are totally blocked by LCO precursor gel. The cross-sectional SEM image (Figure 2f) also shows that the gel was infiltrated inside the microchannels. After removing the excess LCO precursor on the surface by gentle scrape (Figure S5b, Supporting Information), the wood slice was sintered at 700 °C for 2 h in air to form bulk LCO cathode (LCO-1). The obtained bulk LCO cathode (inset in Figure 2d) reproduced the microstructural features of pinewood slice with the diameter of around 30–40 μm (Figure 2d). The cross-sectional SEM images (Figure 2g and Figure S6 in the Supporting Information) also show that the

© 2018 WILEY-VCH Verlag GmbH & Co. KGaA, Weinheim

Ningde Amperex Tech. Exhibit No. 2036
Zhuhai CosMX Battery Co. Ltd. v. Ningde Amperex Tech.
IPR2025-00431, U.S. Patent No. 11,799,131
Page 3 of 9

open vertically aligned microchannels remained throughout in LCO cathode over 1 mm.

To improve the effective mass of active material in as-fabricated LCO bulk cathode for higher areal capacity, the fabrication processes of sol–gel vacuum-assisted infusion and calcination were repeated twice. The mass of obtained LCO cathode (LCO-2) increased notably after the repetitive sol–gel infusion and calcination processes and its density determined by the Archimedes method using ethanol as the medium also increased to 206 mg cm^{-2} correspondingly (Table S1, Supporting Information). As shown in Figure 2h, the diameter of microchannels in the LCO-2 had a considerable reduction and the hole-walls were thickened obviously. The cross-sectional SEM image (Figure 2i) indicated that the open vertical microchannels still remained in the LCO-2 cathode. To further clearly show the continuous microstructure of as-fabricated LCO cathode, SEM characterization combined with focused ion beam (FIB) etching technique was performed on the hole-walls of LCO-1 electrode (Figure S7, Supporting Information). With the FIB etching, the continued LCO walls can be observed and the secondary pores in the walls were revealed by the magnified SEM image (Figure S7d, Supporting Information) as well. The secondary nanopores in the walls resulted from LCO nanoparticle aggregation during the sol–gel process, which is also confirmed by transmission electron microscopy (TEM) image (Figure S8, Supporting Information). The powder X-ray diffraction patterns of the obtained LCO electrodes confirmed the formation of pure phase of $LiCoO_2$ in our wood-templated synthesis (JCPDS: 50–0653) (Figure 2j). To demonstrate the integrity of the LCO without pulverization as the freestanding electrode, the mechanical properties of LCO electrode were investigated showing the flexural strength of 0.45 MPa (Figure S9, Supporting Information) and the time-lapse images from Video S1 (Supporting Information) also show that LCO electrode still retained its integrity after falling down to the desk (Figure S10, Supporting Information).

3D analysis of microstructures inside the obtained bulk LCO cathode was conducted by the X-ray-based microtomography (μCT) to evaluate the influence of vertical microchannels on the tortuosity of the electrode. A control LCO was prepared via pelleting the LCO particles, carbon black additives, and binders into a disk (for details, please see the Experimental Section) for comparison. The gray-level images of cross-sections are obtained by computed tomography (CT) scan. In image processing, a multilevel image threshold method (Otsu's method) is employed to perform the reduction of a gray-level image to a binary image in order to distinguish and recognize the electrochemically active material LCO (white: gray scale intensity: 255) and the void space (black: gray scale intensity 0). The process is repeated in each image of the cross-section and then these binary images are imported into the software VGstudio MAX 2.2 for visualization of the 3D microstructure (Video S2-4, Supporting Information). As shown in **Figure 3**a, reconstructed images show the segmented image and the corresponding radial and transverse cross-sections of the control LCO, LCO-1,

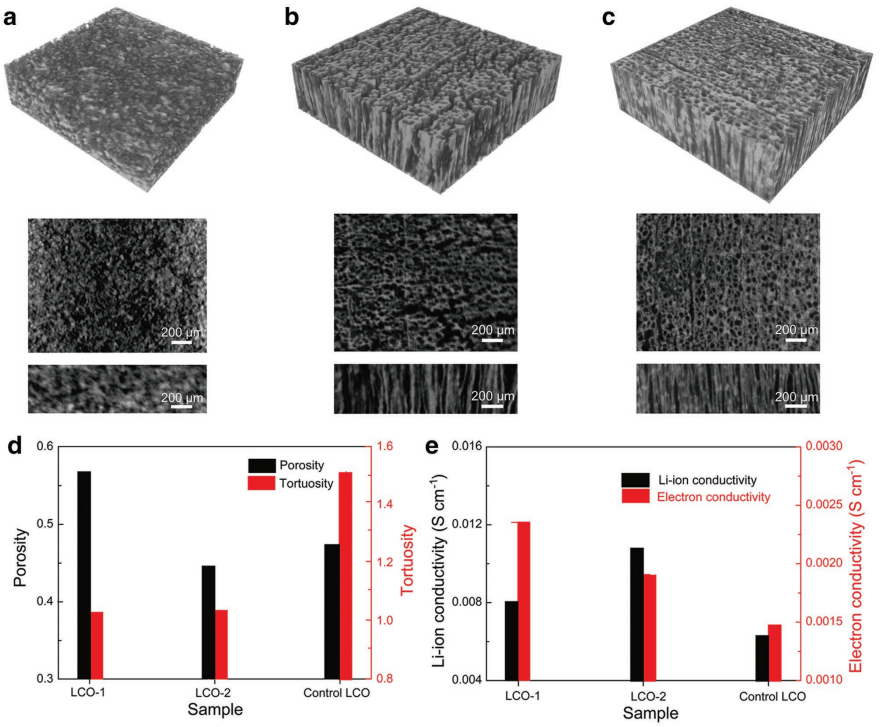

Figure 3. 3D reconstructed LCO cathode by X-ray-based microtomography. a–c) 3D volume rendering of (a) control LCO, (b) LCO-1, and (c) LCO-2 visualized with μCT imaging performed at Y.Cheetah (Y.XLON, Germany) at a 500 nm resolution, respectively. The images included raw segmented image and the corresponding radial and transverse cross-sections of microsamples. The scale bars were 200 μm. d) The comparison of tortuosity and porosity of LCO-1, LCO-2, and control LCO. e) The calculated Li-ion and electron conductivities of LCO-1, LCO-2, and control LCO.

© 2018 WILEY-VCH Verlag GmbH & Co. KGaA, Weinheim

Ningde Amperex Tech. Exhibit No. 2036
Zhuhai CosMX Battery Co. Ltd. v. Ningde Amperex Tech.
IPR2025-00431, U.S. Patent No. 11,799,131
Page 4 of 9

and LCO-2 collected by computed microtomography (CT) scan, respectively. The control LCO sample is consisted of random particle accumulation, indicating no obvious ordered channel for Li-ion transport. In contrast, the vertically aligned channels existed obviously in the LCO-1 and LCO-2 fabricated by wood templating method from the radial and transverse cross-section images, which benefited the Li-ion transport in whole electrode by providing shortened paths. From the radial cross-section image of LCO-1 and LCO-2, it could be observed that the channel size was reduced from 30–40 to 10–20 µm with the increase in the density of LCO.

We determined that the porosity (ε) is the ratio of the void space volume to the electrode volume, which can be obtained by counting voxels in the 3D dataset. In order to quantitatively analyze the ε of 3D reconstructed volume, image segmentation was needed to attribute different gray scale values to different phases. The visualized images (Figure S11, Supporting Information) distinguished the active material (red) from the pores (white). The corresponding pores and active material volume were corrected and processed by MATLAB software. Porosities in these reconstructed structures were derived as 0.500, 0.528, and 0.441 for the control LCO, LCO-1, and LCO-2, respectively. In order to evaluate them with experimental results, the compact densities of electrodes were also measured by the Archimedes' method using ethanol as the medium after compaction (Table S2, Supporting Information). The porosity was obtained as the ratio of compact density to theoretical density of LCO (5.1 g cm^{-3}), which are 0.490, 0.789, and 0.578 for the control LCO, LCO-1, and LCO-2, respectively. The relative errors of the calculations and experimental results in the porosities of LCO-1 and LCO-2 were 33.0% and 23.7%, respectively. The errors were mainly due to the space resolution of µCT at 500 nm in this study, which could not recognize nanoscale pores existed in the walls of LCO electrode (Figure S7, Supporting Information). However, the small space is not the dominant mass transport path for Li ions throughout the whole electrode and therefore the porosities of reconstructed structures are adopted for the lithium ion conductivity analysis.

The tortuosity (τ) is defined by geometrical calculation based on the microstructure of the electrode, which is the ratio of the effective actual path length L_{eff} to the straight-through path length L

$$\tau = \frac{L_{\text{eff}}}{L}$$

where the effective path length is calculated using the distance propagation method with the algorithm. In detail, we adopted the distance propagation method with the so-called "city-block" algorithm[9] (for the details of the evaluation, please see the Supporting Information). From this definition, it is clear that the tortuosity is equal to 1 when channels are straight and perpendicular to the top surface; instead, the curved or inclined channels will lead to a larger tortuosity. The porosity and tortuosity of each sample are plotted in Figure 3d. For the samples LCO-1 and LCO-2, which are fabricated by wood templates, the tortuosity is approximately the same and close to 1 due to the ordered microchannel. In comparison, the tortuosity of control LCO is about 1.5 times larger than that of the samples LCO-1 and LCO-2 due to the random distribution of $LiCoO_2$ particles.

The Li^+ conductive properties should be the key issue to limit the improvement of LIB performance in the ultrathick electrode. It is essential to calculate the effective conductivity of lithium ions ($\sigma_{Li^+}^{\text{eff}}$), which is associated with the ε and τ. Referring to previous research works,[40] the effective conductivity of Li ions is proportional to the ε and inversely proportional to the τ based on the porous media theory

$$\sigma_{Li^+}^{\text{eff}} = \frac{\varepsilon}{\tau}\sigma_{Li^+}^{\text{bulk}} \tag{1}$$

where $\sigma_{Li^+}^{\text{bulk}}$ is the conductivity of Li ions in the electrolyte. Similarly, the effective conductivity of electrons is proportional to the volume fraction of the active material (1-ε) and inversely proportional to the tortuosity

$$\sigma_{e^-}^{\text{eff}} = \frac{1-\varepsilon}{\tau}\sigma_{e^-}^{\text{bulk}} \tag{2}$$

where $\sigma_{e^-}^{\text{bulk}}$ is the conductivity of the electron in the bulk $LiCoO_2$, which is given as 1×10^{-3} S cm^{-1}.[41] Substituting the values of ε, τ, $\sigma_{Li^+}^{\text{bulk}}$, and $\sigma_{e^-}^{\text{bulk}}$ into Equations (1 and 2), the effective conductivity of Li ions and electrons can be obtained, which are plotted in Figure 3e. Compared to the control LCO, the LCO-1 and LCO-2 fabricated by wood templating in the $\approx\varepsilon$ with low τ had much improved Li ionic and electrical conductivities indicating better electrochemical performances. We employ a porous electrode model to give a quantitative analysis of the effect of the tortuosity (τ) on the capacity utilization at different C-rates. The aligned structure primarily affects the transportation of Li^+ ions in the electrolyte, which can be reflected by these two parameters, $D_{Li^+}^{\text{eff}} = \frac{\varepsilon}{\tau^2}D_{Li^+}^{\text{bulk}}$ and $\sigma_{Li^+}^{\text{eff}} = \frac{\varepsilon}{\tau}\sigma_{Li^+}^{\text{bulk}}$. In order to shed light on the effect of the tortuosity, the porosity of the electrode (ε) is set as constant in our simulation (for the details of the model simulation, please see the Supporting Information). The voltage versus the specific capacity curves at different C-rates was simulated. As shown in Figure S12 (Supporting Information), the specific capacity decreased as the tortuosity increased; moreover, the capacity decay becomes more dramatically at the higher C-rate, which was mainly due to the decrease of both the effective diffusivity and the effective conductivity as the tortuosity increased. For the wood-inspired structure with low tortuosity, the transportation performance of Li^+ ions in the electrolyte is enhanced, resulting in a higher discharging capacity in a given C-rate, especially at high C-rate. The results were consistent with the impact of low tortuosity depicted based on the 3D µCT analysis mentioned above.

To evaluate the effect of low tortuosity endowed by wood-inspired ordered structures on the electrochemical performance of ultrathick LCO cathode, the electrochemical tests were performed in half-cells and compared to the control LCO cathode. Figure S13 (Supporting Information) shows the first charge/discharge voltage profiles of LCO-1, LCO-2, and control LCO. Although no conductive carbon existed in LCO-1 and LCO-2 cathodes, both cathodes behaved sufficient electronic conductivity and displayed lower or comparable polarization voltages in comparison to the control LCO cathode, which is consistent with the calculation results of electronic conductivities on the basis of 3D µCT analysis (Figure 3e). However, the larger irreversible capacities were observed for LCO-1 and LCO-2 than that for control LCO (Figure S13, Supporting Information). The

© 2018 WILEY-VCH Verlag GmbH & Co. KGaA, Weinheim

Ningde Amperex Tech. Exhibit No. 2036
Zhuhai CosMX Battery Co. Ltd. v. Ningde Amperex Tech.
IPR2025-00431, U.S. Patent No. 11,799,131
Page 5 of 9

larger irreversible capacity of LCO-1 and LCO-2 can be attributed to the following aspects: (1) LCO-1 and LCO-2 composed of nanoparticles with large specific surface area would have much more side reaction with the electrolyte; (2)the irreversible structural changes of bulk LCO also leaded to the capacity loss; and (3) the main factor resulting in the lower irreversible capacity of control LCO could be the kinetic limitation of side reactions. As shown in Figure S13 (Supporting Information), the charge and discharge capacity of control LCO is much lower than the aligned LCO due to its lower Li^+ ion conductivity. Especially in the charging process, the cell would rapidly reach to the cutoff voltage due to the limitation of Li ionic conductivity, which largely reduce the extent of side reactions in the control LCO resulting in smaller irreversible capacity.

To further investigate the discharge rate improvement induced by the wood-templated microstructures, the LCO cathodes were firstly charged to 4.25 V at 0.05 C and then discharged to 2.5 V at different rates according to previously reported protocol (Figure S14, Supporting Information).[26] The comparison of the obtained specific capacity versus C-rate of LCO cathodes is shown in **Figure 4**a. The control LCO cathode with random microstructures yielded as low capacity utilization as 65% even at the low C-rate of 0.05 C. What is worse, when the rate increased, the capacity of control LCO cathode dropped down rapidly to near zero at 1 C due to the high Li-ion transport resistance in the 1 mm thick electrode. In contrast, the LCO-1 and LCO-2 cathodes both delivered considerable specific capacity with the increase of C-rates and retained > 70% of original capacity at 0.5 C. Even at 1 C, 73.7 and 37.8 mAh g^{-1} can be delivered by LCO-1 and LCO-2, respectively. The ultrathick LCO-2 cathode also exhibited stable cycling at discharging rate of 0.5 C with specific capacity of 64 mAh g^{-1} and areal capacity of 12 mAh cm^{-2} (Figure S15, Supporting Information), implying the robustness of as-constructed vertically aligned microstructures in the electrode during cycling.

The areal capacities of LCO-1 and LCO-2 at different rates were compared as well to show the influence of porosity and mass loading on the performance of as-fabricated ultrathick cathodes. The relevant discharge voltage profiles of LCO-1 and LCO-2 cathodes at different rates are shown in Figure S16 (Supporting Information). Through increasing the areal mass and lowering the porosity of LCO by repeated sol–gel and calcination process, the corresponding areal capacity of LCO-2 (24.5 mAh cm^{-2}) was much higher than that of LCO-1 (13.3 mAh cm^{-2}) in the voltage range between 2.5 and 4.25 V at 0.05 C. Along with the increase of C-rate, the areal capacity of LCO-2 is always nearly twofold of that of LCO-1 (Figure 4d), indicating that the vertically aligned microchannels allowed the high utilization of LCO at the lower porous electrode due to the reduced tortuosity as demonstrated by microtomography analysis. It is worth noting that the areal capacity of LCO-2 dropped unexpectedly to a relatively low value (8.2 mAh cm^{-2}) at 1 C, which is attributed to the large polarization and deterioration

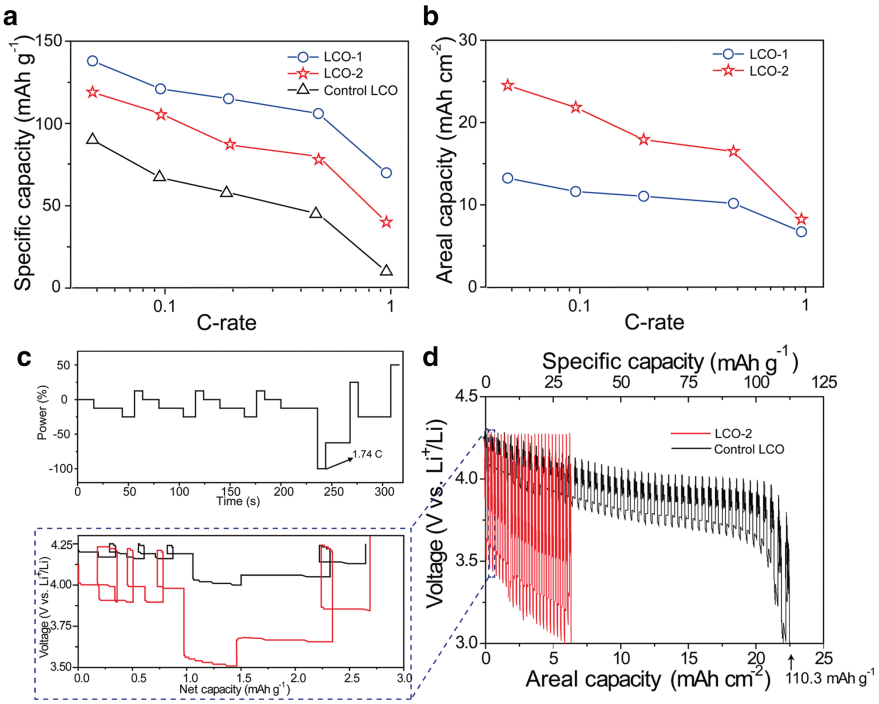

Figure 4. Electrochemical performance and DST test comparison of LCO cathodes. a) The plot of specific capacity versus discharge rate for LCO-1, LCO-2, and control LCO cathodes. b) The plot of areal capacity versus C-rate for LCO-1 and LCO-2. c) The ratio of power versus time profile for the USABC dynamic stress test. d) Voltage versus discharge capacity curves for the LCO-2 and control LCO during tests in which the DST cycle is repeated until the lower voltage limit of 3.0 V is reached. Inset: the magnified initial power cycles showing the lower polarization of the microchannels aligned LCO-2 cathode.

© 2018 WILEY-VCH Verlag GmbH & Co. KGaA, Weinheim

Ningde Amperex Tech. Exhibit No. 2036
Zhuhai CosMX Battery Co. Ltd. v. Ningde Amperex Tech.
IPR2025-00431, U.S. Patent No. 11,799,131
Page 6 of 9

of Li metal anode at such high current density. The cell after the test at high rate of 1 C was further disassembled to study its decay mechanism. As shown in Figure S17a (Supporting Information), the color of Li foil changed to black and a massive mossy-like Li appeared on the surface of Li foil induced by the dendritic growth of Li (Figure S17b, Supporting Information), which mainly hindered the performance of LCO-2 at high rate. On the contrary, the integrity and the vertical microchannel structures of LCO-2 cathode were remained after the test, indicating the good strain tolerance of LCO-2 during high rate delithiation/lithiation processes (Figure S17c and d, Supporting Information). More importantly, in our case, the current density for the thick LCO at 1 C was ≈10 times as high as the traditional cathode, for which there exists a large polarization at the Li metal anode resulting in a sudden capacity decay. Figure S18 a and b shows the voltage profiles and overpotentials of Li plating/stripping at different rates, respectively. It can be seen from Figure S18a (Supporting Information) that the charge–discharge voltage plateaus turn to more and more rough with the increase in C-rate from 0.1 to 2 C. At the same time, the overpotential of stripping/plating increases from 88 to 550 mV accordingly. In particular, at 1 and 2 C, the voltage plateau deteriorated rapidly and the overpotential increased intensively. These factors resulted in a sudden capacity decay due to the serious electrode polarization as shown in Figure 4b. Thus, to further match the performance of thick LCO cathode at a higher rate (over 1 C), the newly designed Li metal anode is desired to improve its rate performance.

Fast charging property is also one of the most important characteristics of the battery applied in electric vehicles (EVs). To demonstrate the superiority of designed structure for fast charging, the charging performance of the aligned LCO was also investigated in comparison to control LCO. The charging voltage profiles of control LCO and LCO-1 at the low rate of 0.05 C are plotted in Figure S19a (Supporting Information). The LCO-1 displays lower or comparable polarization in comparison to that of control LCO cathode due to its sufficient electronic and Li^+ ion conductivity derived from the aligned structure. The comparison of the obtained charge capacity versus C-rate of LCO cathodes is shown in Figure S19b (Supporting Information). The control LCO cathode with random microstructures yielded a low capacity of 82.9 mAh g^{-1} even at the low rate of 0.05 C. What is worse, when the rate increased to 0.2 C, the charge capacity of control LCO cathode dropped rapidly down to 30 mAh g^{-1}. In contrast, the LCO-1 cathode delivered considerable specific charge capacity with the increase of C-rates and retained 84 mAh g^{-1} at 0.2 C. These results further demonstrate the superiority of our aligned electrode with low tortuosity. It is worth noting that in comparison to the discharging rate tests, the highest rate of charging tests is limited to 0.2 C due to the formation of Li dendrites under high charging current density.

To demonstrate that the overall rate performance of wood-inspired bulk LCO cathode is sufficient for practical applications, especially for potentially future EVs, electrochemical performance of LCO cathodes was evaluated through specific drive-cycle test. The DST specified by the United States Advanced Battery Consortium (USABC) is a cycle based on the percentage of peak discharge power. Figure 4c shows the power versus time profile. The test power at each step in profile is selected based on a percentage of the peak power of the battery, which is selected to reach the goal of USABC 2020 EV battery power of 700 W kg^{-1}. The peak power is converted to the charge rate of 1.74 C (for details, please see Experimental Section). The highest charge rate of 0.87 C and maximum discharge rate of 1.74 C in the DST are retained 8s. Started with a fully charged process, the DST was run continuously from 100% state of charge at 4.25 V to 0% at 3 V over several cycles in a discharge process.

As shown in the voltage–capacity curves in Figure 4d, obvious differences could be seen between the wood-inspired LCO cathode and control LCO cathode. On one hand, the specific capacity of LCO electrode with vertically aligned microchannels was 110.3 mAh g^{-1} when the lower cutoff voltage reached to 3.0 V, which was threefold more than that of control LCO cathode (31.6 mAh g^{-1}). On the other hand, the areal capacity of the wood-templated LCO cathode could reach up to 22.7 mAh cm^{-2} in one-time dynamic discharge, far exceeding the areal capacity of commercial LCO cathode (5–6 mAh cm^{-2}). Aside from these, the wood-templated LCO had much lower polarizations of voltage, especially at high discharge rate in comparison to that of control LCO (the magnified voltage–time response in Figure 4d). Thus, from the representative drive-cycle test, an ultrathick electrode at the millimeter scale with an inspiring areal capacity is appealing for practical operation at continuous 1–2C rates.

Thick cathode has been an effective strategy to significantly improve the energy density of battery by increasing the ratio of active materials to the nonactive materials in liquid and solid system.[42] To compare the performance of thick electrode in solid and liquid battery, the mass and volumetric energy density based on the cell were calculated according to our data and the reported data in the literature (Table S4, Supporting Information). As shown in Figure S20 (Supporting Information), the mass energy density of thick cathode in solid system without diffusion limitation is higher than that in liquid system. However, the thick cathode in liquid system exhibits higher volumetric energy density because the separator is much thinner than the solid electrolyte.

In summary, we proposed a bio-templated route to fabricate ultrathick LCO electrode with continuous vertically aligned microchannels inside to reduce the tortuosity for improving rate performance. The 3D microstructures of as-fabricated LCO cathodes were comprehensively analyzed by the X-ray-based microtomography demonstrating the efficiency of wood templating to reduce the tortuosity and improve Li-ion conductivity in bulk LCO cathodes. As a result, the ultrathick LCO cathode (1 mm) with continuously aligned microchannels could deliver a high areal capacity of 22.7 mAh cm^{-2} under the dynamic discharge test, which far exceeds the areal loading capacity of the commercial LCO cathode. Although we have a large percentage of pore volume in our electrodes with low volumetric capacity, we believe future study of decreasing the pore volume in these vertical channels can result in significant improvement. Benefiting from the abundant and widespread natural woods on the earth, the ultrathick electrodes based on wood templating sol–gel process will be promising alternatives to fabricate high specific energy/power LIBs at low cost.

© 2018 WILEY-VCH Verlag GmbH & Co. KGaA, Weinheim

Ningde Amperex Tech. Exhibit No. 2036
Zhuhai CosMX Battery Co. Ltd. v. Ningde Amperex Tech.
IPR2025-00431, U.S. Patent No. 11,799,131
Page 7 of 9

Experimental Section

Fabrication of LCO Cathodes: For the fabrication of wood-templated LCO cathode, a series of pinewood blocks were provided from Linyi Dafuwood Co., Ltd. The blocks were cut into slices of 1.5 mm thickness with an area of 15 mm × 15 mm using a bench saw (Model: Difan 180) (Figure S3, Supporting Information). The wood slices were boiled in dilute ammonia solution (5 wt%) for 5 h to get rid of lignin inside and enhance the channel connectivity of templates for the following sol infusion. The lignin-extracted pinewood slices were washed by deionized water followed by pure ethanol three times, respectively, and then dried for the following use. The LCO electrodes were synthesized via a sol–gel vacuum-assisted infusion and calcination process. Lithium nitrate (99.9%) and cobalt nitrate (99%) were purchased from Alfa Aesar and used as received. The sol of LCO was prepared according to previous report.[43] In brief, lithium nitrate (50 mmol) and cobalt nitrate salts (50 mmol) were dissolved in 30 mL of distilled water and then the solution was mixed with polyacrylic acid aqueous solution (1.8 g, 50 wt%). The pH value of the solution was adjusted to be 1–2 by nitric acid with constant stirring to yield the LCO sol. Then the wood slices were immersed into the LCO sol under the vacuum at 90 °C for 72 h to evaporate the solvent. This procedure yielded $LiCoO_2$ gel within the microchannels of the wood template. After removing the excess LCO precursor on the surface, the wood template was removed by sintering the sample in air at the temperature of 700 °C for 2 h with a slow heating rate of 0.5 °C min^{-1}. To obtain the LCO electrode of higher areal mass, the steps of sol–gel vacuum-assisted infusion and the calcination process were repeated. For the fabrication of control LCO electrode, an *N*-methyl-2-pyrrolidone slurry of the commercial $LiCoO_2$ active material mixed with carbon conductive additive and polyvinylidene difluoride binder was firstly dried in an oven of 80 °C and then pressed into a pellet by a hydraulic machine (YLJ-CSP-40A, Hefei Kejing Material Technology Co., Ltd.).

Electrochemical Testing: The LCO electrodes were tested in a detached type half-cell (Provided by Hefei Kejing Material Technology Co., Ltd., Figure S21, Supporting Information) coupled with Li foil as the anode on a Biologic VMP-3 potentiostat using the electrolyte of 1.0 M $LiPF_6$ in EC:DMC:EMC = 1:1:1 wt% with the polypropylene separator (Celgard 2340). The weight ratio of electrolyte injection to the active materials is ≈4g/2g. The rate capability of the cells was tested based on charge–discharge cycling of simultaneous rate change. To further investigate the discharge rate capacity, the cells were started with being charged at a low rate of 0.05 C to 4.25 V and then the voltage was retained until the current dropped to below 0.025 C. The discharge rate was changed from 0.05 to 1 C as noted in the main text. The cutoff voltage was set up at 2.5 V. For the long-term cycling, the cells were first activated at 0.1 C for three cycles and then kept the constant charge and discharge at 0.5 C for the following cycles. The rate performance of lithium was tested in a symmetric cell using two Li foils in 1.0 M $LiPF_6$ in EC/EMC/DMC (1:1:1). The mount of Li deposition is set as 20 mAh g^{-1} and the relevant current density of 1 C rate is 20 mA g^{-1}. The rate varied from 0.1 to 2 C. To further investigate the charge rate capacity, the cells with an activation were charged at a low rate of 0.05 C to 4.25 V followed by constant voltage charging until the current dropped to below 0.025 C and then were discharged to 2.5 V. Subsequently, the cells were charged at a series of rates from 0.05 to 0.2 C by a constant-current followed a constant-voltage charging process. The discharge rate is constant 0.1 C. The charging capacity is defined as the portion in the constant current process.

Dynamic Stress Test: The DST was performed according to the USABC Electric Vehicle Battery Test Procedures Manual. The currents were calculated based on a 700 W kg^{-1} battery pack with half of a 12.5 µm alumina current collector for the cathode, half of a 12.5 µm copper current collector for the anode, a 25 µm porous separator, carbonate-based electrolyte, and a 0.85 packaging factor. Before the test, the electrodes were charged at a rate of C/20, followed by a constant voltage step at 4.25 V until the current dropped to below C/40. The cutoff voltage of discharge process was 3.0 V.

Characterizations: SEM images were performed on JEOL-6700F to carry out the morphologies of the wood and the bulk LCO electrode. TEM (Hitachi H-7650) was employed to characterize the nanoscale morphologies of the LCO particles synthesized by sol–gel method. Powder X-ray diffraction (PXRD) patterns were performed on a Philips X'Pert PRO SUPER X-ray diffractometer equipped with graphite monochromatized Cu Kα radiation. The DualBeam 820 FIB/SEM (FEI Helios Nanolab 600i) was employed to confirm the continuous walls of microchannels in the LCO cathode. The Micro-CT conducted on Y.Cheetah (Y.XLON, Germany) provided 3D information on the electrode architecture with a resolution high enough to distinguish the microscale pores. Three-point bending tests were performed on an Instron 5565A universal testing machine. The LCO electrode was carefully cut into sheets with a length of 10 mm, a width of 5 mm, and a thickness of 1 mm for test. The loading rate was 0.1 mm min^{-1}.

Supporting Information

Supporting Information is available from the Wiley Online Library or from the author.

Acknowledgements

L.-L.L. and Y.-Y.L. contributed equally to this work. H.-B.Y., Y.C., and S.-H.Y. supervised the research. L.-L.L., Z.-J.X., and T.-W.Z. carried out the experiments and characterizations. L.L.L., Z.-J.X., H.-B.Y., Y.C., and S.-H.Y. conceived the figures and tables. L.L.L. and H.-B.Y. had designed and drawn schematic illustration of the preparation process. Y.-Y.L. and Y.N. carried out the calculation and evaluation of the structure by X-ray-based microtomography. L.L.L., Z.-J.X., T.-W.Z., F.Z., T.M., H.-B.Y., Y.C., and S.-H.Y. analyzed the data and co-wrote the manuscript. The authors acknowledge the funding support from the National Natural Science Foundation of China (Grant Nos. 21431006, 51571184, 21501165), the Foundation for Innovative Research Groups of the National Natural Science Foundation of China (Grant No. 21521001), the National Basic Research Program of China (Grant Nos. 2014CB931800, 2013CB931800), the Users with Excellence and Scientific Research Grant of Hefei Science Center of CAS (Grant Nos. 2015HSC-UE007, 2015SRG-HSC038), the Strategic Priority Research Program of the Chinese Academy of Sciences (Grant No. XDB22040502), the Defense Industrial Technology Development Program (Grant No. JCKY2016208B012), Key Research Program of Frontier Sciences, CAS (Grant No. QYZDJ-SSW-SLH036), and the Chinese Academy of Sciences (Grant No. KJZD-EW-M01-1).

Conflict of Interest

The authors declare no conflict of interest.

Keywords

areal capacity, bio-inspired materials, $LiCoO_2$, tortuosity, ultrathick electrodes, wood

Received: November 18, 2017
Revised: January 19, 2018
Published online:

[1] D. Larcher, J. M. Tarascon, *Nat. Chem.* **2015**, *7*, 19.
[2] S.-Y. Chung, J. T. Bloking, Y.-M. Chiang, *Nat. Mater.* **2002**, *1*, 123.
[3] C. Liu, F. Li, L.-P. Ma, H.-M. Cheng, *Adv. Mater.* **2010**, *22*, 28.

© 2018 WILEY-VCH Verlag GmbH & Co. KGaA, Weinheim

Ningde Amperex Tech. Exhibit No. 2036
Zhuhai CosMX Battery Co. Ltd. v. Ningde Amperex Tech.
IPR2025-00431, U.S. Patent No. 11,799,131
Page 8 of 9

[4] K. Mizushima, P. C. Jones, P. J. Wiseman, J. B. Goodenough, *Mater. Res. Bull.* **1980**, *15*, 783.
[5] A. K. Padhi, K. S. Nanjundaswamy, J. B. Goodenough, *J. Electrochem. Soc.* **1997**, *144*, 1188.
[6] H. Zheng, J. Li, X. Song, G. Liu, V. S. Battaglia, *Electrochim. Acta* **2012**, *71*, 258.
[7] G. Zhou, L. Li, C. Ma, S. Wang, Y. Shi, N. Koratkar, W. Ren, F. Li, H.-M. Cheng, *Nano Energy* **2015**, *11*, 356.
[8] B. Dunn, J. W. Long, D. R. Ronson, *Electrochem. Soc. Interface* **2008**, *17*, 49.
[9] Y.-C. K. Chen-Wiegart, R. DeMike, C. Erdonmez, K. Thornton, S. A. Barnett, J. Wang, *J. Power Sources* **2014**, *249*, 349.
[10] M. Moradi, Z. Li, J. Qi, W. Xing, K. Xiang, Y.-M. Chiang, A. M. Belcher, *Nano Lett.* **2015**, *15*, 2917.
[11] P. V. Braun, J. Cho, J. H. Pikul, W. P. King, H. Zhang, *Curr. Opin. Solid State Mater. Sci.* **2012**, *16*, 186.
[12] F. Shen, W. Luo, J. Dai, Y. Yao, M. Zhu, E. Hitz, Y. Tang, Y. Chen, V. L. Sprenkle, X. Li, L. Hu, *Adv. Energy Mater.* **2016**, *6*, 1600377.
[13] P. A. Johns, M. R. Roberts, Y. Wakizaka, J. H. Sanders, J. R. Owen, *Electrochem. Commun.* **2009**, *11*, 2089.
[14] C.-J. Bae, C. K. Erdonmez, J. W. Halloran, Y.-M. Chiang, *Adv. Mater.* **2013**, *25*, 1254.
[15] Y. Li, K. K. Fu, C. Chen, W. Luo, T. Gao, S. Xu, J. Dai, G. Pastel, Y. Wang, B. Liu, J. Song, Y. Chen, C. Yang, L. Hu, *ACS Nano* **2017**, *11*, 4801
[16] J. W. Long, B. Dunn, D. R. Rolison, H. S. White, *Chem. Rev.* **2004**, *104*, 4463.
[17] H. Zhang, X. Yu, P. V. Braun, *Nat. Nanotechnol.* **2011**, *6*, 277.
[18] I. V. Thorat, D. E. Stephenson, N. A. Zacharias, K. Zaghib, J. N. Harb, D. R. Wheeler, *J. Power Sources* **2009**, *188*, 592.
[19] C. Chen, Y. Zhang, Y. Li, J. Dai, J. Song, Y. Yao, Y. Gong, I. Kierzewski, J. Xie, L. Hu, *Energy Environ. Sci.* **2017**, *10*, 538.
[20] K. C. Smith, P. P. Mukherjee, T. S. Fisher, *Phys. Chem. Chem. Phys.* **2012**, *14*, 7040.
[21] J. H. Pikul, H. Gang Zhang, J. Cho, P. V. Braun, W. P. King, *Nat. Commun.* **2013**, *4*, 1732.
[22] Y. S. Hu, P. Adelhelm, B. M. Smarsly, S. Hore, M. Antonietti, J. Maier, *Adv. Funct. Mater.* **2007**, *17*, 1873.
[23] Y. G. Guo, Y. S. Hu, W. Sigle, J. Maier, *Adv. Mater.* **2007**, *19*, 2087.
[24] S. Behr, R. Amin, Y. Chiang, A. Tomsia, *Ceram. Forum Int.* **2015**, *2*, 39.
[25] J. Billaud, F. Bouville, T. Magrini, C. Villevieille, A. R. Studart, *Nat. Energy* **2016**, *1*, 16097.
[26] J. S. Sander, R. M. Erb, L. Li, A. Gurijala, Y. M. Chiang, *Nat. Energy* **2016**, *1*, 16099.
[27] Z. Schnepp, W. Yang, M. Antonietti, C. Giordano, *Angew. Chem., Int. Ed.* **2010**, *49*, 6564.
[28] J. W. Galusha, M. R. Jorgensen, M. H. Bartl, *Adv. Mater.* **2010**, *22*, 107.
[29] H. Yao, G. Zheng, W. Li, M. T. McDowell, Z. Seh, N. Liu, Z. Lu, Y. Cui, *Nano Lett.* **2013**, *13*, 3385.
[30] N. Huebsch, D. J. Mooney, *Nature* **2009**, *462*, 426.
[31] H. B. Yao, Z. H. Tan, H. Y. Fang, S. H. Yu, *Angew. Chem., Int. Ed.* **2010**, *49*, 10127.
[32] L.-B. Mao, H.-L. Gao, H.-B. Yao, L. Liu, H. Cölfen, G. Liu, S.-M. Chen, S.-K. Li, Y.-X. Yan, Y.-Y. Liu, S.-H. Yu, *Science* **2016**, *354*, 107.
[33] S. Deville, E. Saiz, R. K. Nalla, A. P. Tomsia, *Science* **2006**, *311*, 515.
[34] E. Munch, M. E. Launey, D. H. Alsem, E. Saiz, A. P. Tomsia, R. O. Ritchie, *Science* **2008**, *322*, 1516.
[35] S. Bose, C. Das, *Ceram. Int.* **2015**, *41*, 4070.
[36] J. Pan, J. Pan, X. Cheng, X. Yan, Q. Lu, C. Zhang, *J. Eur. Ceram. Soc.* **2014**, *34*, 249.
[37] C. Chen, Y. Zhang, Y. Li, Y. Kuang, J. Song, W. Luo, Y. Wang, Y. Yao, G. Pastel, J. Xie, *Adv. Energy Mater.* **2017**. *7*, 1700595.
[38] T. Ohzuku, A. Ueda, M. Nagayama, Y. Iwakoshi, H. Komori, *Electrochim. Acta* **1993**, *38*, 1159.
[39] N. Janani, S. Ramakumar, L. Dhivya, C. Deviannapoorani, K. Saranya, R. Murugan, *Ionics* **2011**, *17*, 575.
[40] G. Inoue, M. Kawase, *J. Power Sources* **2017**, *342*, 476.
[41] M. Nishizawa, S. Yamamura, *Chem. Commun.* **1998**, *16*, 1631.
[42] Y. Kato, S. Hori, T. Saito, K. Suzuki, M. Hirayama, A. Mitsui, M. Yonemura, H. Iba, R. Kanno, *Nat. Energy* **2016**, *1*, 16030.
[43] G. Li, J. Zhang. *Appl. Surf. Sci.* **2012**, *258*, 7612.

© 2018 WILEY-VCH Verlag GmbH & Co. KGaA, Weinheim

View publication stats